Journal of Geophysical Research – Solid Earth

Supporting Information for

The role of pyroxenite in basalt genesis: Melt-PX, a melting parameterization for mantle pyroxenites between 0.9 and 5 GPa

Sarah Lambart[1]†, Michael B. Baker[1], and Edward M. Stolper[1]

[1]Division of Geological & Planetary Sciences, California Institute of Technology, Pasadena, CA 91125, USA.

†Present Address: Department of Earth and Planetary Sciences, University of California Davis, One Shields Avenue, Davis, California 95616, USA

Contents of this file

Additional Supporting Information (Files uploaded separately)

Melt-PX.XSLM
Table S1

Introduction

The supporting information complements the main text by:

- Providing additional detailed descriptions (in Text sections S1 to S5 and in Figs. S1 to S14)
- Providing the complete data set of compositions and parameters used in the parameterization and in subsequent calculations (Tables S1 and S2)

The Supporting Information also consists of the Microsoft Excel spreadsheet entitled Melt-PX.XLSM. This software calculates the degree of melting of two pyroxenite compositions at a specified pressure and temperature. The software can also calculate the adiabatic decompression-melting path of a two-lithology mantle (i.e., pyroxenite + peridotite). The user specifies the major-element composition of the pyroxenite and its mass fraction in the assemblage, the modal fraction of clinopyroxene in the subsolidus peridotite, and the potential temperature of the mantle.

Text S1. pMELTS calculations

Although the equations in Melt-PX describing $T_{5\%}$ (the temperature at 5% melt), $T_{cpx\text{-}out}$ (the temperature at the disappearance of clinopyroxene), and F (the percentage of melt) as functions of P, T, and composition (X) are not thermodynamically based, our use of pMELTS [*Ghiorso et al.,* 2002] minimizes the hazards of a totally arbitrary functional form.

pMELTS is calibrated in the system SiO_2-TiO_2-Al_2O_3-Fe_2O_3-Cr_2O_3-FeO-MgO-CaO-Na_2O-K_2O-P_2O_5-H_2O between 1 and 4 GPa and was optimized to model liquid-solid and solid-solid phase relations in peridotitic systems. For this reason, pMELTS does not accurately reproduce the results of pyroxenite partial melting. Nevertheless, pMELTS does calculate an equilibrium assemblage of phases by minimizing an appropriate potential energy, subject to constraints on bulk composition; on temperature, pressure, or volume; enthalpy or entropy; and optionally on oxygen fugacity (fO_2). Thus, we can use pMELTS to calculate an internally consistent set of equilibrium assemblages as a function of P and T for compositions ranging from peridotite to basalt in order to explore the relationships between bulk composition and melt fraction as P and T change.

Below, we list the choices and constraints that we used in our pMELTS calculations: (1) Calculations were made at $fO2$ = FMQ-1 (i.e., the fayalite-magnetite-quartz buffer minus one log unit, close to the oxygen fugacity in graphite-Pt double capsule experiments [*Laporte et al.*, 2004]). (2) We used the corrected version of the garnet model [*Berman and Koziol*, 1991]. (3) We did not include Cr_2O_3 in the bulk compositions used for these calculations. Incorporation of Cr_2O_3 in solid phases is oversimplified in pMELTS (i.e., it is not included in pyroxene and garnet [*Asimow et al.*, 1995]); as a result, the stability field of spinel is strongly overestimated when Cr_2O_3 is included in the calculation. (4) MnO was also not included because pMELTS is not calibrated for this element. (5) Even though K_2O is handled incorrectly in the subsolidus assemblage when feldspar is absent [*Asimow and Ghiorso*, 1998], we chose to include potassium as a major element in all supersolidus calculations because this leads to pMELTS $T_{5\%}$ estimates more consistent with the experimental data and to greater numerical stability. [Note that the bulk K_2O content in all our pMELTS calculations was kept low and constant (0.025 mol. %).]

Starting with the composition MIX1G [*Hirschmann et al.*, 2003], we independently varied the following compositional parameters: the mole fractions of Na_2O and SiO_2, the Mg#, the molar CaO/Al_2O_3 ratio, and the forsterite (Fo) and quartz (Qz) components (calculated using

the expressions in *O'Hara* [1972]) to generate 36 related compositions. Using pMELTS, we calculated $T_{5\%}$ for each of these compositions at pressures of 1–5 GPa in order to identify simple correlations between $T_{5\%}$ and the various compositional variables and pressure.

MIX1G was chosen as the base composition for this exercise because: (1) its composition is close to the average of 431 pyroxenite compositions compiled from the literature (Fig. S1), and (2) pMELTS qualitatively reproduces its solidus and super-solidus phase relations (see Fig. 1 in the main text). MIX1G is a silica deficient pyroxenite (Figs. S1-S2; [*Hirschmann et al.,* 2003]) and both the experiments and the calculations indicate that, at 2 and 2.5 GPa, the solidus assemblage is olivine (ol) + clinopyroxene (cpx) + garnet (gt) + spinel (sp); that at 5 GPa, the solidus assemblage is ol + gt + cpx (the stability of gt increases with pressure); and that ol is the first phase to disappear during melting at all three pressures. There are, however, important quantitative differences between the experimental phase relations and those estimated by pMELTS—for example, pMELTS overestimates the stability of gt at low pressure at the expense of sp due to the absence of Cr_2O_3 in the bulk composition (as noted above, including Cr_2O_3 greatly over-stabilizes spinel). pMELTS also strongly underestimates the stability of cpx at high pressure—at 5 GPa, it predicts the disappearance of cpx at $F = 32\%$; the actual disappearance of *cpx* in the experiments is close to $F = 75\%$ (Table S1). At a given P and T in the super-solidus region of the phase diagram, pMELTS does not reliably estimate the melt percentage for MIX1G, emphasizing the need for a parameterization that is able to accurately predict *P-T-F* relationships for pyroxenite compositions. Specifically, pMELTS overestimates the size of the melting interval, especially at high pressures, by both overestimating the liquidus temperature and underestimating the solidus temperature (see Fig. 1 in the main text).

Text S2. Determination of experimental $T_{5\%}$ and $T_{cpx\text{-}out}$ values

As described in the main text, our parameterization models the melting of pyroxenites from *5%* to the disappearance of cpx, and since F is described in part as a function of $T_{5\%}$ and $T_{cpx\text{-}out}$, calibrating the model involves calculating $T_{5\%}$ and $T_{cpx\text{-}out}$ values for pyroxenite melting experiments in our literature database. For each literature data set (where a "data set" is all experiments performed on a given composition at a given pressure), we plotted the experimental temperatures as a function of melt percentage (calculated using the compositions of solid and liquid phases in each experiment and the mass balance program of *Albarède and Provost* [1977]), and then used a quadratic regression to estimate T at $F = 5\%$ (Fig.

S3). To estimate $T_{cpx\text{-}out}$, when *cpx* is the liquidus phase, we used these same quadratic fits and calculated T at F = 100% (i.e., $T_{cpx\text{-}out}$). When *cpx* is not the liquidus phase, and there were insufficient *cpx*-bearing experiments to define a robust relationship between T and modal cpx, we estimated $T_{cpx\text{-}out}$ by averaging T from the last experiment with residual cpx and T from the next higher temperature experiment. When there were sufficient data, we used the evolution of the proportion of *cpx* as a function of melt fraction to calculate $F(T_{cpx\text{-}out})$ and and then used the quadratic fit to estimate $T_{cpx\text{-}out}$ for this value of $F(T_{cpx\text{-}out})$ (Fig. S4; the proportions of residual solid phases decrease in an approximately linear fashion with increasing F [e.g., *Baker and Stolper*, 1994; *Lambart et al., 2013*; *Pickering-Witter and Johnston*, 2000]). For example, 4 GPa experiments on GA2 [*Spandler et al.*, 2008] show that the solid assemblage is cpx + gt between from F = 19% and F = 49%. Clinopyroxene disappears in the interval between 49% and 89% melt. Using a linear regression between the modal abundances of *cpx* and F (based on mass balance), we estimated that *cpx* disappears at F = 85.3% (Fig. S4). Then using the quadratic fit shown in Fig. S3, we calculated that $T_{cpx\text{-}out}$ = 1512°C. To estimate the uncertainties on $T_{5\%}$ and $T_{cpx\text{-}out}$, we used the uncertainties on the calculated melt fractions and 1σ uncertainties on each experimental temperature (±10°C). Then we estimated the "upper" and "lower" $T_{5\%}$ and $T_{cpx\text{-}out}$ values from the quadratic fits at +1σ and -1σ on both T and F (Fig. S3). The calculated $T_{5\%}$ and $T_{cpx\text{-}out}$ values and their uncertainties are reported in Table S1. Note that a quadratic relationship between T and F is consistent with experimental observations [*Lambart et al., 2009a*; *Pertermann and Hirschmann,* 2003a; *Sobolev et al.,* 2007; *Spandler et al.,* 2008], and with the results of pMELTS calculations on various pyroxenite bulk compositions (Fig. S5).

Text S3. Factors that control $T_{5\%}$

As briefly discussed in section S1 (and in the main text), pMELTS cannot be used to quantitatively predict the phase relations of pyroxenites. Nevertheless, it provides an internally self-consistent set of phase relations that can be used to explore those parameters that closely correlate with $T_{5\%}$. Based on the results of 143 pMELTS calculations (the reason for 143 vs. 180 calculations is discussed in the main text), $T_{5\%}$ is negatively correlated with Na_2O content and positively correlated with Mg#. At constant pressure, the effects of bulk Na_2O content and Mg# on $T_{5\%}$ are approximately linear, however, the magnitude of these effects increases with increasing pressure, i.e., the slopes of the lines in Fig. 3a-b (main text) steepen as pressure increases. Although the effect of bulk Na_2O on $T_{5\%}$ is accentuated in the pMELTS calculations at high pressure due to the non-pressure dependent partitioning of Na between

clinopyroxene and melt [e.g., *Jennings and Holland,* 2015], the effect is still seen, as we show below, in the experimental data. In the 5 GPa pMELTS calculations, the decrease in $T_{5\%}$ with increasing bulk CaO/Al_2O_3 (Fig. S6a) is due to the decrease in the jadeite component in the clinopyroxene (due to a decrease in Al/Na) and this, in turn, increases the incompatibility of Na, and consequently the Na_2O content of the melt. However, as noted by *Putirka et al.* [2003], pMELTS does not accurately predict the mass fraction of the jadeite component in clinopyroxene at high pressures, and no correlation is observed between CaO/Al_2O_3 and $T_{5\%}$ in the pMELTS calculations at 1 and 3 GPa (Fig. S6a). For this reason, we did not include a CaO/Al_2O_3 term in our parameterization of $T_{5\%}$.

Although $T_{5\%}$ is not correlated with bulk SiO_2 content (Fig. S6b), there is a peak in $T_{5\%}$ values for the synthetic compositions with close to 47 mol.% silica at pressures between 2 and 5 GPa. Significantly, these are compositions that plot close to the En-CaTs-Di plane in the CMAS system [*Herzberg*, 2006] and, at pressures above the appearance of garnet, this plane is a thermal divide [*Kogiso et al.*, 2004a; *Lambart et al.*, 2013]. *Kogiso and Hirschmann* [2006] have suggested that for bulk compositions with the same alkali content and Mg#, bimineralic pyroxenites will have slightly higher solidus temperatures than pyroxenites that consist of three or more major crystalline phases; although they note that the effect is likely to be relatively small and easily overwhelmed by changes in bulk alkali content and Mg#. To investigate the potential magnitude of the thermal divide on near-solidus temperatures, we constructed a series of compositions based on MIX1G by adding or subtracting a Qtz or Fo component [*O'Hara*, 1972]. We then projected these compositions onto the Fo-CaTs-Qz plane from Di and calculated, using pMELTS, the evolution of $T_{5\%}$ along the two compositional joins (Fig. S7). At 1 GPa, garnet in not stable in the solid assemblage and thus the CaTs-En-Di plane does not represent a thermal divide—and indeed, we observe almost no change in $T_{5\%}$ as a function of distance from the thermal divide along either compositional join. In contrast, between 2 and 5 GPa, we observe an increase in $T_{5\%}$ of up to 270°C close to the thermal divide for the synthetic data set. This effect is more than an order of magnitude larger than that inferred by *Kogiso and Hirschmann* [2006]. To test whether this large ΔT effect is an artifact of pMELTS, we plotted $T_{5\%}$ values from our experimental data set as a function of distance from the thermal divide in Di-Fo-CaTs-Qz space (Fig. S8). Although there is a monotonic increase in experimental $T_{5\%}$ values as ΔQz changes from positive to negative, there is no obvious maximum in the $P > 2$ GPa trends in the vicinity of the thermal divide. Figure S8 supports the

conclusions of *Kogiso and Hirschmann* [2006] that the influence of the thermal divide on pyroxenite solidus temperatures is relatively small.

Text S4. Tests of the model calibration

We have tested our expression for $T_{5\%}$ (equation 2 in the main text) using experimental data not included in the calibration of the model (see section 3.5, main text). Calculated F-test statistics [*Snedecor and Cochran*, 1989] for equation (2) vs. equations for $T_{5\%}$ with one less parameter indicate that dropping a parameter significantly decreases the accuracy of the model. As a further test of our equations, we have plotted the differences between calculated and experimental values for $T_{5\%}$, $T_{cpx\text{-}out}$, and F ($\Delta T_{5\%}$, $\Delta T_{cpx\text{-}out}$, and ΔF, respectively) as functions of the variables (e.g., P, Mg#, "alk", etc.) used to parameterize equations (2), (3), and (1) (main text), as well as other variables (e.g., oxide mol.% SiO_2, CaO/Al_2O_3, etc.) not used in the equations. No significant correlations were observed between $\Delta T_{5\%}$, $\Delta T_{cpx\text{-}out}$, and ΔF and any of these variables (Figs. S9–S11). There are also no obvious systematic offsets about any of the three $\Delta = 0$ lines for SD or SE pyroxenites. This suggests that our equations include the significant variables that influence $T_{5\%}$, $T_{cpx\text{-}out}$, and F for all the pyroxenite compositions in the experimental data set.

Text S5. Adiabatic decompression of a two-lithology mantle

We used the equations of *Phipps Morgan* [2001] coupled with the melting parameterization of *Katz et al.* [2003] for fertile peridotite and Melt-PX (this study) for pyroxenites to calculate $(dT/dP)_S$ and $(dF/dP)_S$ for a parcel of mantle undergoing adiabatic upwelling that consists of two lithologies (peridotite and pyroxenite). Each increment of melting is calculated by following a reversible adiabatic path with complete melt extraction. Melting and decompression are assumed to occur isentropically, thermal equilibrium is maintained between both lithologies, and both lithologies are chemically isolated. Melts from each lithology are continuously extracted and mixed along the melting column. Crustal thickness (tc) is calculated using equation (6) in Appendix A of *White et al.* [1992], which accounts for compaction of the melting region in response to melt extraction and assumes a mean crustal density of 2900 kg/m^3. Equation (6) [*White et al.,* 1992] was modified so that the term that corrects for compaction took into account mass loss due to melt extraction if one or both lithologies were melting):

$$tc = \frac{1}{\rho_l \cdot g}\left[\emptyset \int \frac{F^A}{1-(\emptyset F^A+(1-\emptyset)F^B)}\,dP + (1-\emptyset)\int \frac{F^B}{1-(\emptyset F^A+(1-\emptyset)F^B)}\,dP\right] \quad \textbf{(S.1)}$$

where Φ is the mass fraction of lithology A and ρ_l is density of the melt. We stopped the calculations when the mantle column has upwelled to the base of the crust as determined by equation S.1 (i.e., when the pressure at the base of the crust, $P_c = P$, where P_c is equal to $tc \cdot g \cdot \rho_l$). This approach differs from that of *Asimow et al.* [1997] and *Brown and Lesher* [2014] who introduced the term (1–*F*) in the calculation of $-(dF/dP)_S$ that directly accounts for the decreasing mass of the source due to melt extraction. In both treatments, fractional melting is considered as a two-step process: (1) isentropic melt generation followed by (2) melt extraction; both treatments give very similar results in terms of volume of magma produced and oceanic crustal thicknesses generated (Eric Brown, personal communication).

For those cases where a high mantle potential temperature (T_P) and a low final pressure of melting (P_f) lead to the exhaustion of clinopyroxene in the pyroxenite while the mantle is still upwelling and undergoing melting, Melt-PX offers two options: (1) To account for the drop in melt productivity beyond *cpx-out* [observed experimentally in pyroxenites at low pressures; *Lambart et al.*, 2009a], productivity of the pyroxenite can be set to a value of 0.3%/°C after the disappearance of clinopyroxene. (2) Melt productivity can also simply be extrapolated based on the curve defined for temperatures between $F = 5\%$ and $F(T_{cpx\text{-}out})$. Note that in our calculations the drop in melt productivity does not appear to have a large effect on calculated crustal thicknesses. For the case of Iceland discussed in the main text, the mass fraction of MIX1G necessary to produce 20 km of crust decreases from 0.194 (using option 1) to 0.19 (using option 2). It is also important to note, that based on the parameterization presented here, many pyroxenites (e.g., eclogites) will only reach *cpx*-out under conditions involving both a high mantle potential temperature and a low final pressure of melting. This is a rather unusual combination (although one that occurs at Iceland) in that, in nature, a high T_P is usually coupled with a higher final pressure of melting (e.g., Hawaii).

For a given potential temperature, there are four separate conditions for an upwelling parcel of mantle that consists of two distinct lithologies:

1. $\boldsymbol{T < T^A_{solidus}}$ **and** $\boldsymbol{T < T^B_{solidus}}$**:** In this case, neither lithology is melting and *dT*/*dP* follows the bulk solid mantle adiabat:

$$\frac{dT}{dP} = \frac{\alpha T}{\rho C_p} \text{ with } C_p = \emptyset C_p^A + (1-\emptyset)C_p^B \text{ and } \rho = \emptyset\rho^A + (1-\emptyset)\rho^B \quad \textbf{(S.2)}$$

where C_p is the heat capacity, α is the thermal expansivity, ρ^A and ρ^B are the density of the solid lithologies A and B, *and* Φ is as defined for equation S.1; note that α is assumed to be equal for both lithologies.

2. $\boldsymbol{T > T^A_{solidus}}$**,** $\boldsymbol{T < T^A_{liquidus}}$**, and** $\boldsymbol{T < T^B_{solidus}}$: Only A is melting. The effect of this is to cool B, delaying the onset of its melting, but enhancing the melt productivity of A [*Hirschmann and Stolper,* 1996; *Phipps Morgan*, 2001; *Sleep*, 1984; *Stolper and Asimow,* 2007]. Note that in most cases, the pyroxenite lithology will start to melt first within an ascending parcel of lithologically heterogeneous mantle, but both situations can occur (see Section 5.1 in the main text and Fig. S12). The equation for the temperature evolution during perfect fractional melting in this interval is:

$$dT = \left(\frac{\partial T}{\partial F}\right)^A_P dF^A + \left(\frac{\partial T}{\partial P}\right)^A_F dP \qquad \textbf{(S.3)}$$

where $\left(\frac{\partial T}{\partial P}\right)^A_F dP$ is the evolution of the temperature of the source with pressure and $\left(\frac{\partial T}{\partial F}\right)^A_P dF^A$ is the reciprocal term of the isobaric productivity of the lithology A [*Asimow et al.*, 1997]. A's productivity is given by:

$$-\left(\frac{dF}{dP}\right)_S = \frac{\left(\frac{\partial T}{\partial P}\right)^A_F - \frac{\alpha T}{\rho C_p}}{\emptyset\frac{T\Delta S^A_f}{C_p} + \left(\frac{\partial T}{\partial F}\right)^A_P} \qquad \textbf{(S.4)}$$

where ΔS_f is the entropy of fusion of lithology A. Note that our approach differs from that in *Phipps Morgan* [2001]—there $(\partial T/\partial F)_P$ and $(\partial T/\partial P)_F$ were assumed to be constant. However, to correctly model polybaric fractional melting we need to know how the isobaric melt productivity evolves during fractional melting—i.e., how the properties of the residue evolve as the composition of the residue changes. Since it is not yet possible to accurately calculate partial melt compositions of pyroxenites as a function of *T*, *P*, and *X*, our parameterization, Melt-PX, is based on the results of batch melting experiments and this will likely yield estimates of melt production that are higher than those expected during fractional fusion.

3. $\boldsymbol{T > T^A_{solidus}}$**,** $\boldsymbol{T < T^A_{liquidus}}$**, and** $\boldsymbol{T > T^B_{solidus}}$: Both lithologies are melting. *dF/dP* is controlled by the melting functions of both A and B. Because both lithologies are assumed to be in thermal equilibrium, $dT/dP = (dT/dP)^A$ given in equation (S.3). Bulk productivity is given by:

$$\left(\frac{dF}{dP}\right)_S = \emptyset \left(\frac{dF}{dP}\right)_S^A + (1-\emptyset)\left(\frac{dF}{dP}\right)_S^B \quad \textbf{(S.5)}$$

and the individual productivities are:

$$-\left(\frac{dF}{dP}\right)_S^A = \frac{\frac{C_p}{T}\left(\frac{\partial T}{\partial P}\right)_F^A - \frac{\alpha}{\rho} + (1-\emptyset)\Delta S_f^B \frac{\left[\left(\frac{\partial T}{\partial P}\right)_F^A - \left(\frac{\partial T}{\partial P}\right)_F^B\right]}{\left(\frac{\partial T}{\partial F}\right)_P^B}}{\emptyset \Delta S_f^A + (1-\emptyset)\Delta S_f^B \frac{\left(\frac{\partial T}{\partial F}\right)_P^A}{\left(\frac{\partial T}{\partial F}\right)_P^B} + \frac{C_p}{T}\left(\frac{\partial T}{\partial F}\right)_P^A} \quad \textbf{(S.6)}$$

$$\text{and } \left(\frac{dF}{dP}\right)_S^B = \left(\frac{dF}{dP}\right)_S^A \frac{\left(\frac{\partial T}{\partial F}\right)_P^A}{\left(\frac{\partial T}{\partial F}\right)_P^B} + \frac{\left(\frac{\partial T}{\partial P}\right)_F^A - \left(\frac{\partial T}{\partial P}\right)_F^B}{\left(\frac{\partial T}{\partial F}\right)_P^B} \quad \textbf{(S.7)}$$

4. $T > T^A_{liquidus}$ and $T > T^B_{solidus}$: Only B is melting; A has been exhausted from source. *dF/dP* and *dT/dP* reduce to the single lithology melting functions of B. B's productivity is given by:

$$-\left(\frac{dF}{dP}\right)_S = \frac{\left(\frac{\partial T}{\partial P}\right)_F^B - \frac{\alpha T}{\rho_B C_p^B}}{\frac{T\Delta S_f^B}{C_p^B} + \left(\frac{\partial T}{\partial F}\right)_P^B} \quad \textbf{(S.8)}$$

and the temperature change as a function of *P* is:

$$\frac{dT}{dP} = \left(\frac{\partial T}{\partial P}\right)_F^B - \frac{\left(\frac{\partial T}{\partial F}\right)_P^B \left(\left(\frac{\partial T}{\partial P}\right)_F^B - \frac{\alpha T}{\rho_B C_p^B}\right)}{\frac{T\Delta S_f^B}{C_p^B} + \left(\frac{\partial T}{\partial F}\right)_P^B} \quad \textbf{(S.9)}$$

However, none of our calculations ever reached this fourth stage. A final possibility is that A starts to melt before B and that B reaches its liquidus before A reaches its liquidus. We have not considered this case, since for mixtures of pyroxenite and peridotite it seems like an unlikely scenario.

Values assigned to the parameters in these calculations can be found in Table S2 (although the densities of the pyroxenites KG2, M5-103, and MIX1G are not tightly constrained, varying their values between the two end-member values, 3550 kg/m^3 (G2) and 3300 kg/m^3 (fertile peridotite) [*Shorttle and Maclennan*, 2011], does not significantly affect the results of the calculations). Integration begins at P_0, the pressure of the deeper of the two solidii, and stops when $P = Pc$ (the pressure at the base of the crust), with the pressure decrement taken as 0.1 MPa. Figures S13, S14, and Fig. 10 in the main text present *P-T* paths for five different

pyroxenite compositions and for different fractions of pyroxenite in an upwelling mantle with a potential temperature of 1450°C; Figs. S13 and S14 also show how the melting percentages and the isentropic productivities of the pyroxenite and the peridotite evolve along the adiabatic path used to calculate the crustal thicknesses presented in Fig. 9 (main text).

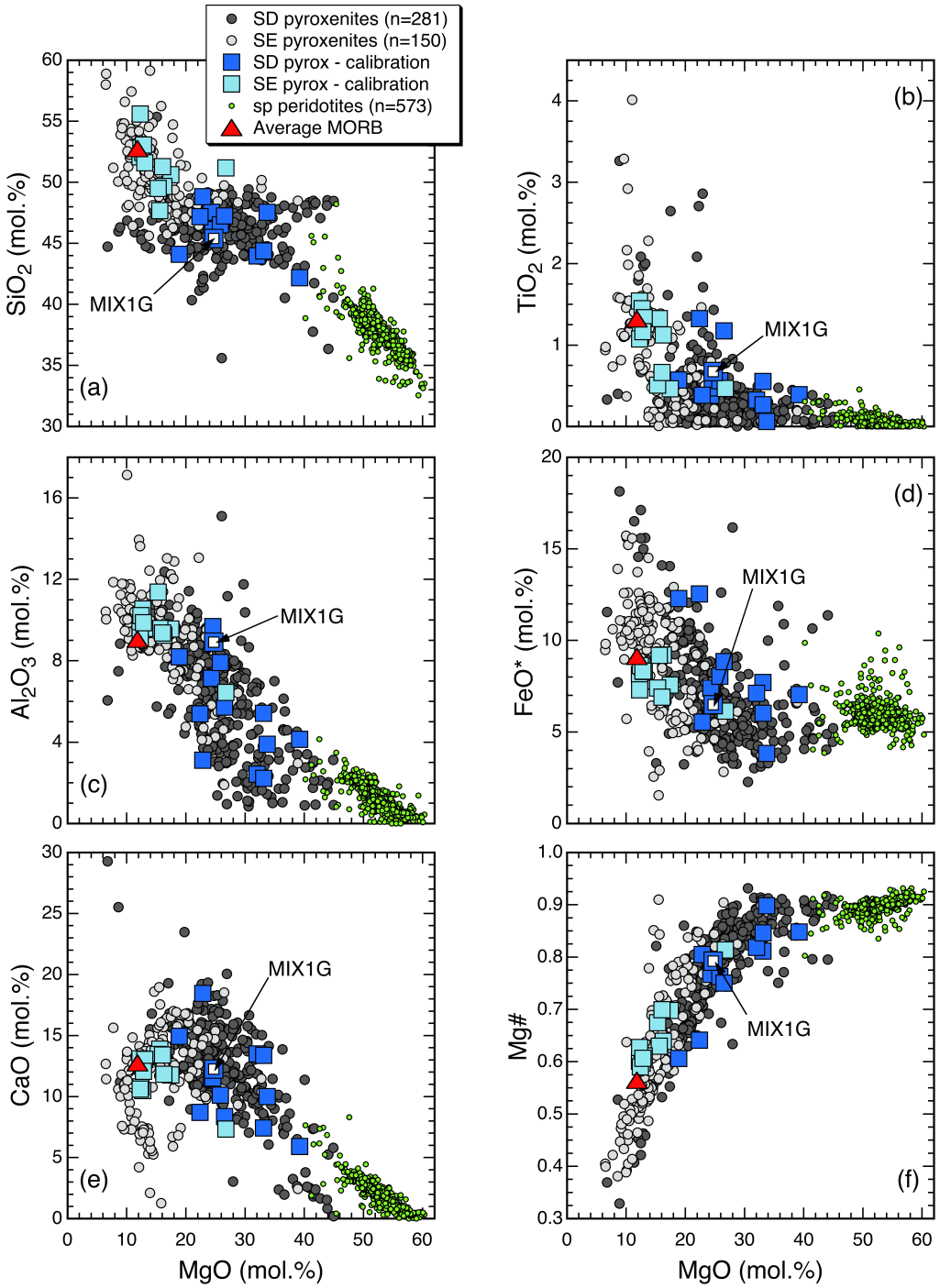

Figure S1. Oxide contents (in mol.%) of natural pyroxenites from ophiolites and alpine-type massifs, gneissic and granulitic massifs, and xenoliths [*Lambart et al.*, 2013 and references therein], spinel peridotites [*Herzberg et al.*, 1988], and average MORB [*Gale et al.*, 2013]. See text for the definition of silica deficient (SD) and silica excess (SE); pyroxenite compositions whose experimental phase relations were used in the parameterization are shown in two shades of blue (see Table S1 for compositions); Mg# is molar Mg/(Mg+Fe*), where Fe* = all Fe as FeO.

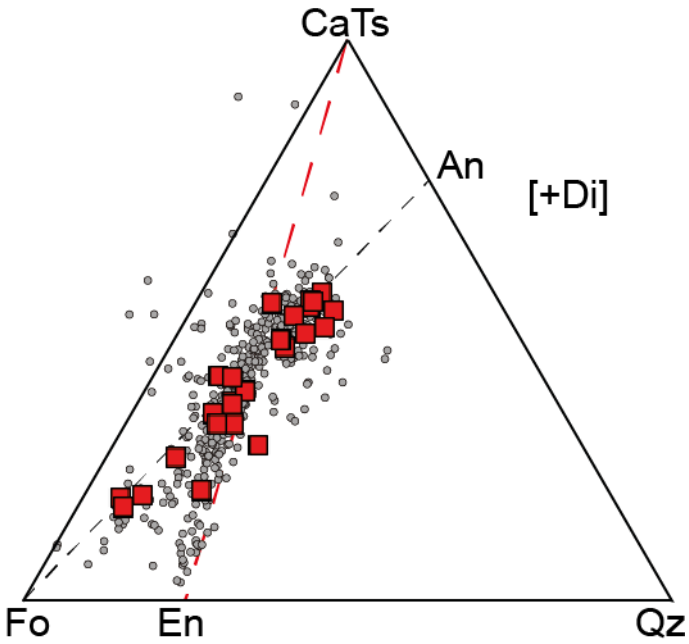

Figure S2. Natural pyroxenites from ophiolites and alpine-type massifs, gneissic and granulitic massifs, and xenoliths [grey circles; *Lambart et al.*, 2013 and references therein] compared to the experimental bulk compositions used in calibrating the parameterization (large red squares; compositions are listed in Table S1). All compositions are projected from Di (diopside) onto the plane CaTs (Ca Tschermak's molecule, $CaAl_2SiO_6$) - Fo (forsterite) - Qz (quartz), using the method of *O'Hara* [1972]. Silica-deficient (SD) and silica-excess (SE) pyroxenites are located on the left and right sides, respectively, of the CaTs–En join (red dashed line).

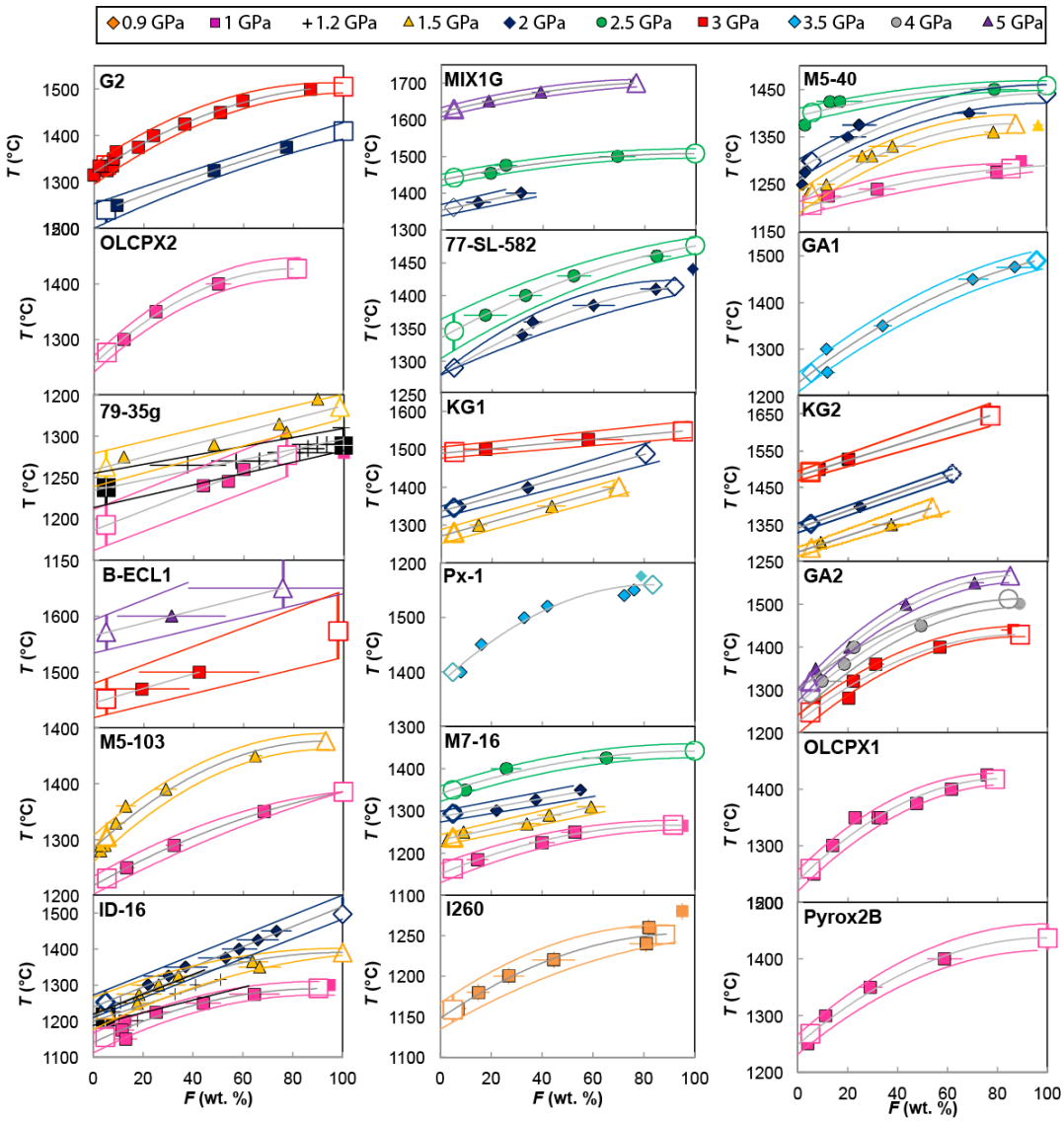

Figure S3. Temperature vs. melt-fraction curves (in wt.%) for pyroxenites used to calibrate $T_{5\%}$. Solid symbols are the experimental data (symbols outlined in black represent experiments that contain cpx and non-outlined symbols represent cpx-free experiments). Error bars are 2σ uncertainties. When not visible, errors are smaller than the size of the symbol. Grey curves denote the quadratic functions that best match the experimental data subject to the constraint that melt fraction remains constant or increases throughout the interval $F = 0$ to F at cpx-out. These curves are used to estimate $T_{5\%}$ and $T_{cpx\text{-}out}$ (open symbols; where $T_{cpx\text{-}out}$ is the temperature at cpx-out). Colored curves describe the ±2σ bounds. The differences between $T_{5\%}$ and $T_{cpx\text{-}out}$ estimated from the grey curves and from these colored lines define the uncertainties on $T_{5\%}$ and $T_{cpx\text{-}out}$, respectively. References are: G2 [*Pertermann and Hirschmann*, 2003a; b]; MIX1G [*Hirschmann et al.*, 2003; *Kogiso et al.*, 2003]; M5-40 and M7-16 [*Lambart et al.*, 2009a; 2012; 2013]; 77SL-582 [*Keshav et al.*, 2004]; GA1 [*Yaxley and Green*, 1998]; KG1 and KG2 [*Kogiso et al.*, 1998]; B-ECL1 [*Kogiso and Hirschmann*, 2006]; Px-1 [*Sobolev et al.*, 2007]; GA2 [*Spandler et al.*, 2008]; Pyrox2B, OLCPX1, and OLCPX2 [*Kogiso and Hirschmann*, 2001]; M5-103 [*Lambart et al.*, 2009a]; ID-16 [*Draper and Johnston*, 1992]; I260 [*Whitaker et al.*, 2007]; 79-35g [*Bartels et al.*, 1991].

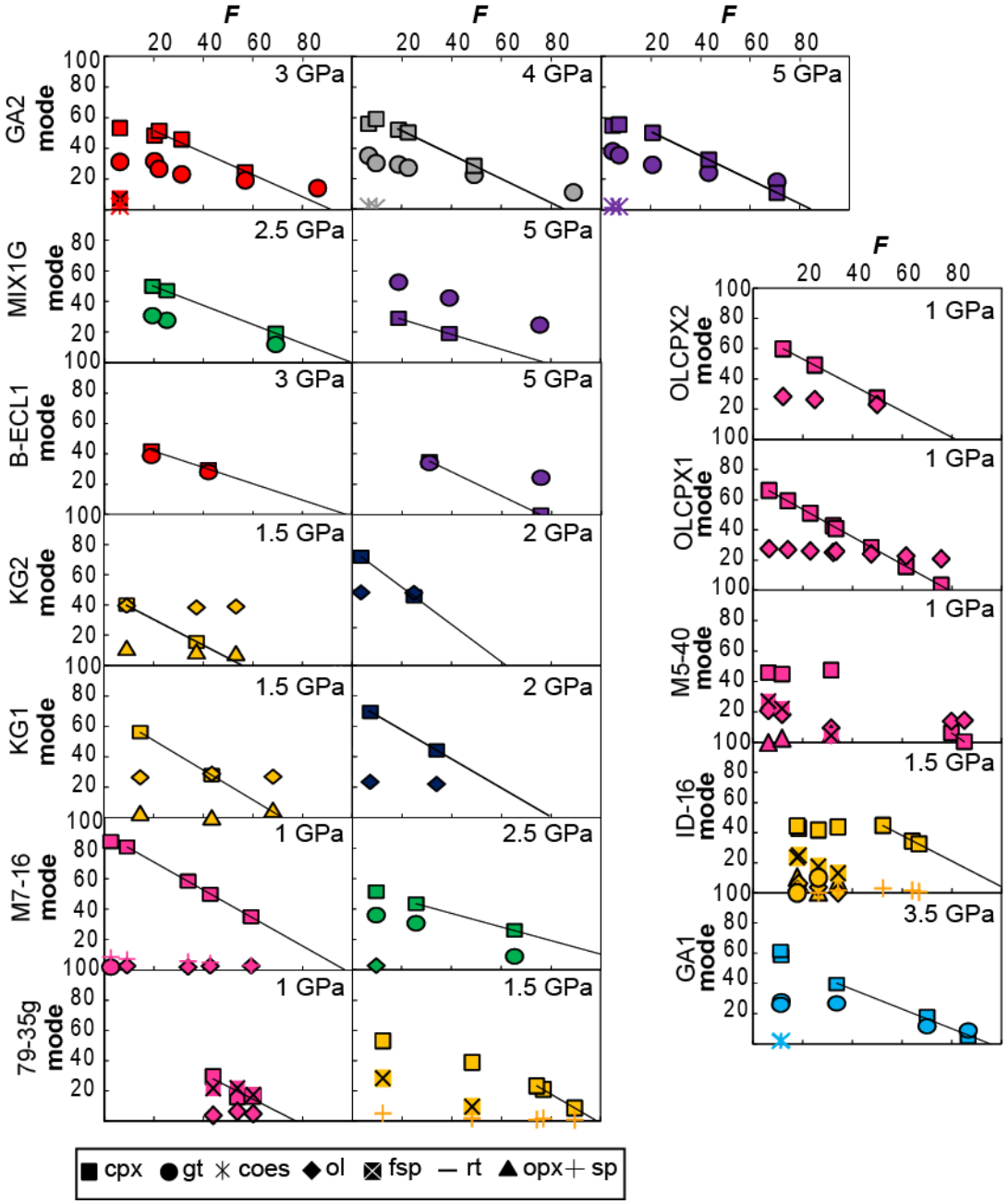

Figure S4. Proportions of solid phases (wt.%) as a function of the proportion of melt, *F* (wt.%). The straight lines are best-fit lines calculated for cpx using those experiments on a given bulk composition where cpx coexists with a fixed phase assemblage; the best-fit lines are used to estimate $F(T_{cpx\text{-}out})$. These values of $F(T_{cpx\text{-}out})$ are then used in conjunction with the melt fraction curves in Fig. S3 to calculate $T_{cpx\text{-}out}$ (see Table S1 and Text S2 for details). Symbols are given in the inset.

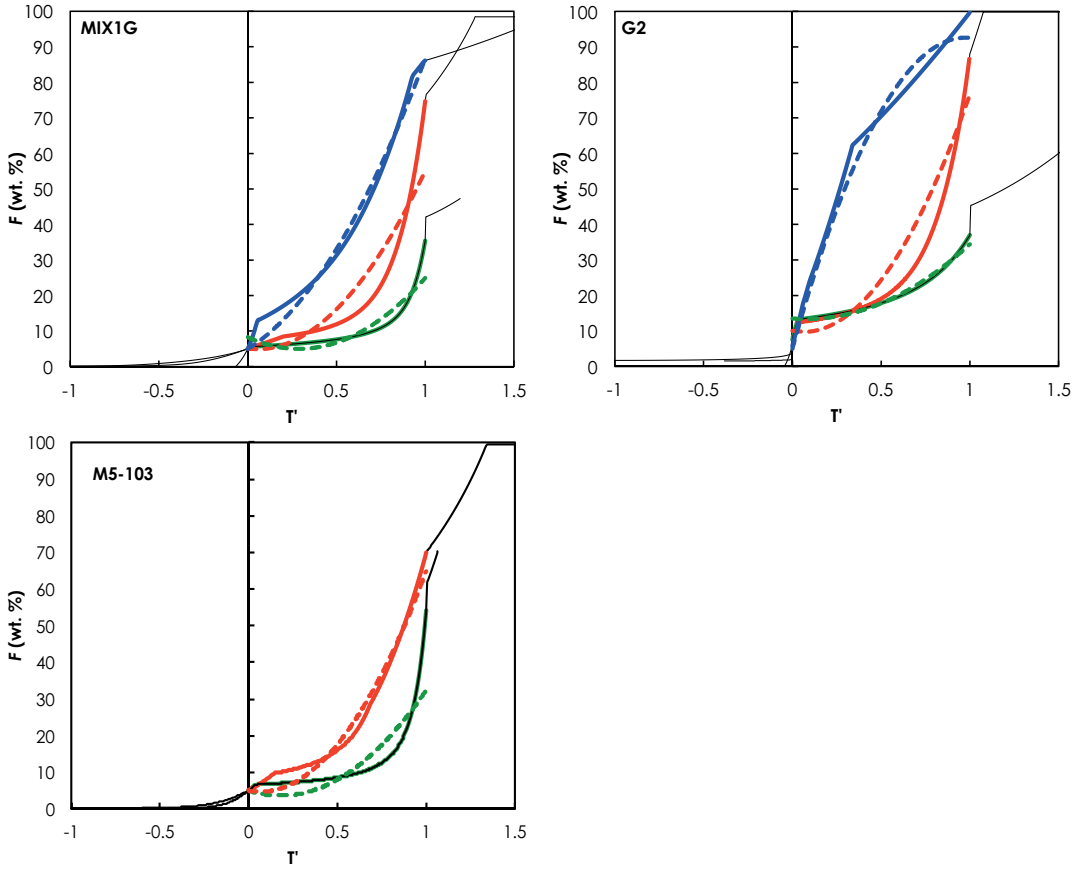

Figure S5. *F* vs. *T'*, where $T' = (T-T_{cpx\text{-}out})/(T_{cpx\text{-}out}-T_{5\%})$ for the compositions MIX1G, G2, and M5-103 at 1, 3, and 5 GPa calculated with pMELTS (solid lines; the solid colored portions of the lines denote *F* values between 5% and *F* at cpx-out; blue = 1GPa, red = 3GPa, green = 5GPa). The compositions of these three pyroxenites cover much of the compositional spread in our experimental database. The dashed lines are the quadratic relationships that best fit the pMELTS results between *F* = 5% and $F(T_{cpx\text{-}out})$. pMELTS calculations for M5-103 at 1 GPa crashed before $T_{cpx\text{-}out}$ was reached.

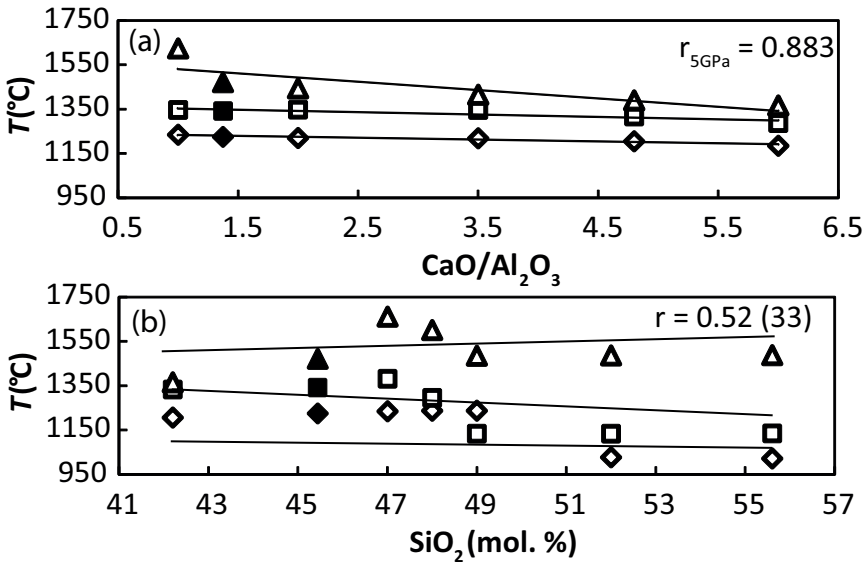

Figure S6. $T_{5\%}$ calculated for MIX1G and associated synthetic compositions using pMELTS at 1 GPa (diamonds), 2 GPa (squares) and 5 GPa (triangles) vs. (a) the molar CaO/Al_2O_3 ratio, and (b) the SiO_2 content of the bulk composition (in mol.%). The initial composition MIX1G is showed by the filled symbols. In (a), r_{5GPa} is the correlation coefficient between CaO/Al_2O_3 and $T_{5\%}$ at 5 GPa. In (b), r is the average of the correlation coefficients calculated at each pressure; the 1σ deviation (in parentheses) is given in terms of the least unit cited.

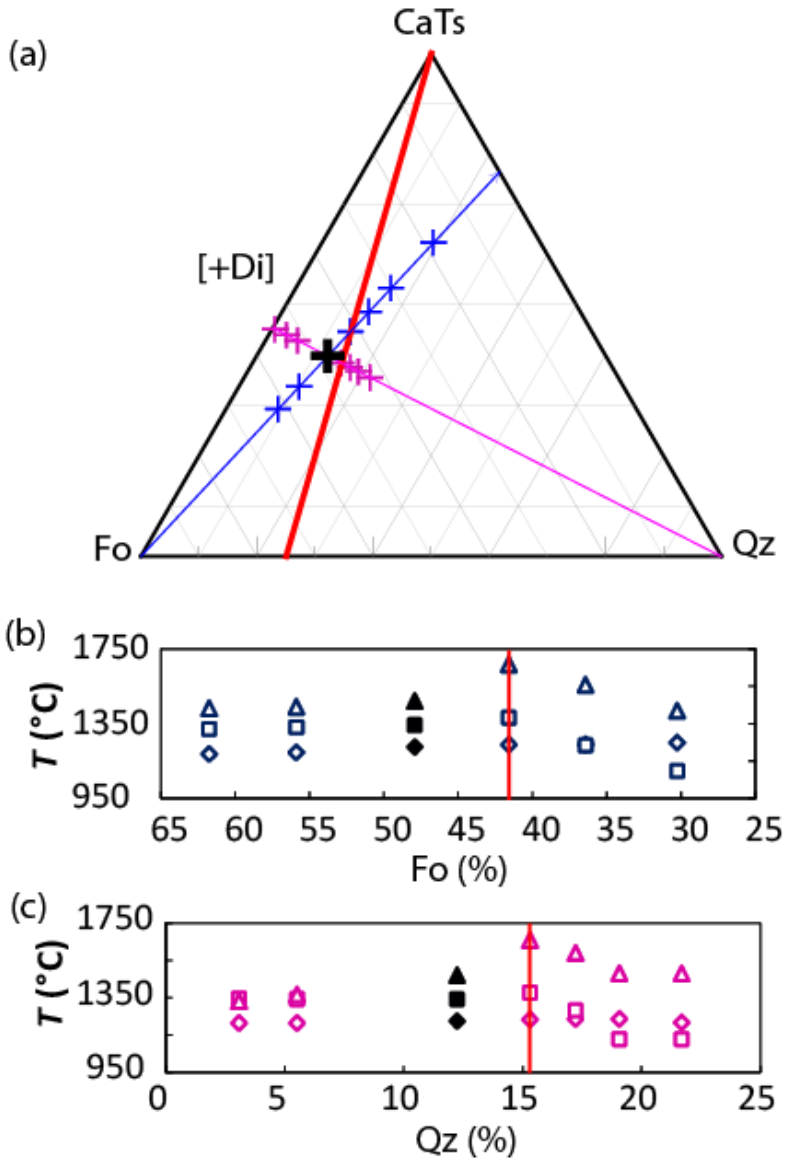

Figure S7. (a) Composition MIX1G (black cross) and derivative compositions (blue and purple crosses) projected from Di (diopside) onto the plane CaTs (Ca Tschermak's molecule, $CaAl_2SiO_6$) - Fo (forsterite) - Qz (quartz), using the method of *O'Hara* [1972]. The derivative compositions were constructed by adding or subtracting Fo or Qz components to or from MIX1G; the thermal divide (red line) is defined by the plane CaTs-Di-En (enstatite). Panels (b) and (c) show the variations in $T_{5\%}$ for MIX1G and the derivative compositions along lines that include the points Fo and MIX1G and Qz and MIX1G, respectively. The symbols in (b) and (c) are the same as those in Fig. S6. The red lines represent the thermal divide. The filled black symbols are for the composition MIX1G.

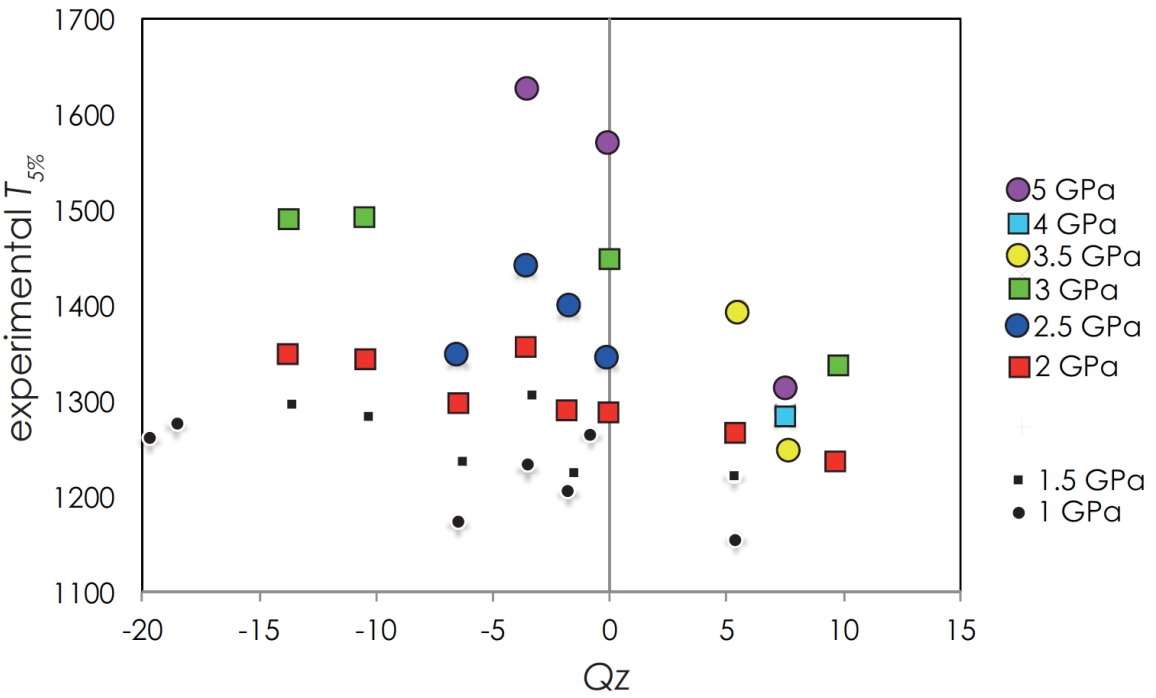

Figure S8. Experimentally determined $T_{5\%}$ values for bulk pyroxenite compositions in our experimental database as a function of each composition's normative Qz content when projected into the tetrahedron Qz - Wo (wollastonite) - Al_2O_3 - En, using the method of *O'Hara* [1972]. The thermal divide in this tetrahedron is defined by the plane Wo-Al_2O_3-En; compositions in this plane have 0% Qz.

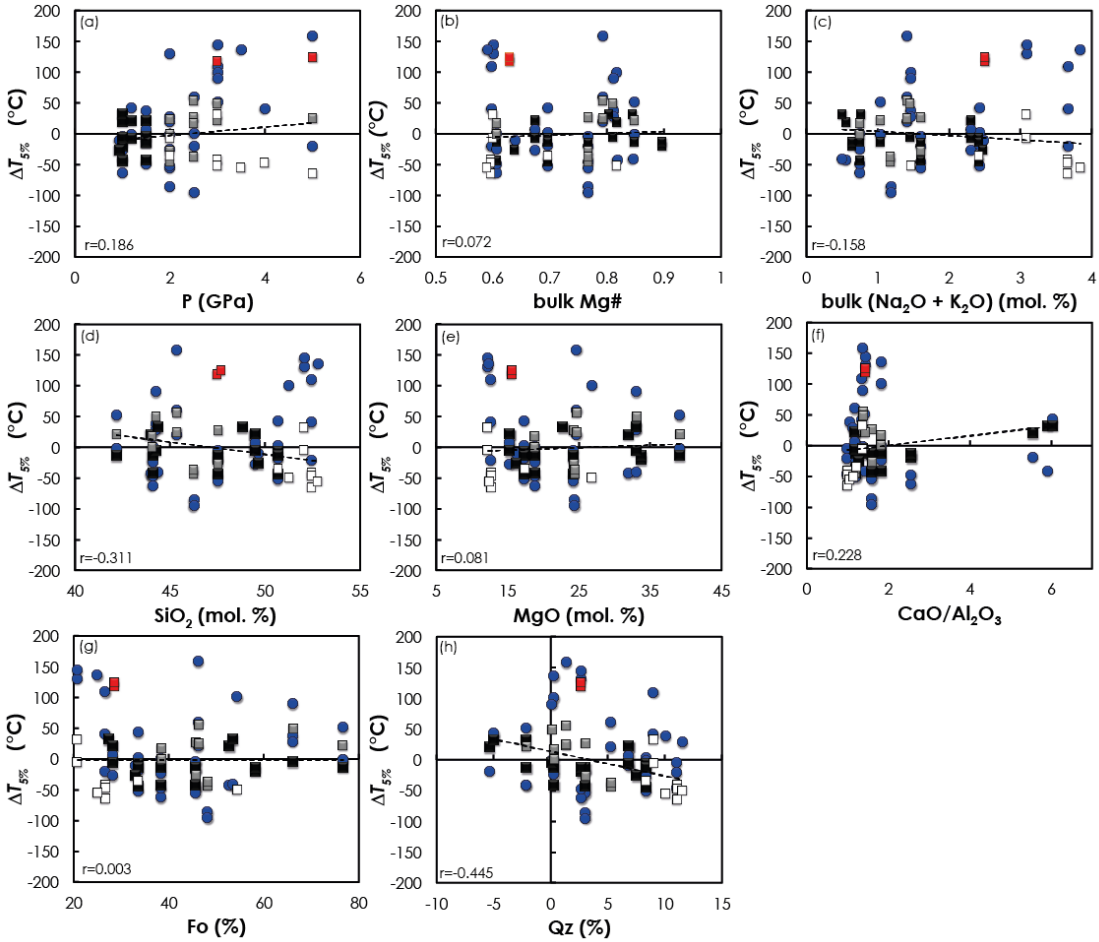

Figure S9. $\Delta T_{5\%}$ (experimental $T_{5\%}$ – calculated $T_{5\%}$) vs. **(a)** *P*, **(b)** bulk Mg#, **(c)** bulk (Na_2O + K_2O), **(d)** bulk SiO_2, **(e)** bulk MgO, **(f)** bulk molar CaO/Al_2O_3, **(g)** Fo content, and **(h)** Qz content; all oxides values are in mol.%. Fo and Qz are the normative forsterite and quartz contents in the tetrahedron Qz - Di (diopside) - CaTs (Ca Tschermak's molecule, $CaAl_2SiO_6$) - Fo, calculated using the method of *O'Hara* [1972]. Square symbols are $\Delta T_{5\%}$ values calculated using Melt-PX; black squares are for sets of experiments performed at < 1.7 GPa, white squares, above 1.7 GPa on SE pyroxenites, grey squares, above 1.7 GPa on SD pyroxenites (1.7 GPa reflects a convenient pressure divide—the thermal divide appears at ~1.7 GPa); red squares are experiments performed at 3 and 5 GPa on the bimineralogic eclogite B-ECL1 [*Kogiso and Hirschmann*, 2006]; sets of experiments denote all experiments performed on a single bulk composition at one pressure. Dashed lines are least-squares fits to the $\Delta T_{5\%}$ points; r is the correlation coefficient between $\Delta T_{5\%}$ calculated with our parameterization and each parameter. Blue circles are $\Delta T_{5\%}$ calculated using pMELTS and were not included in the least-squares fits.

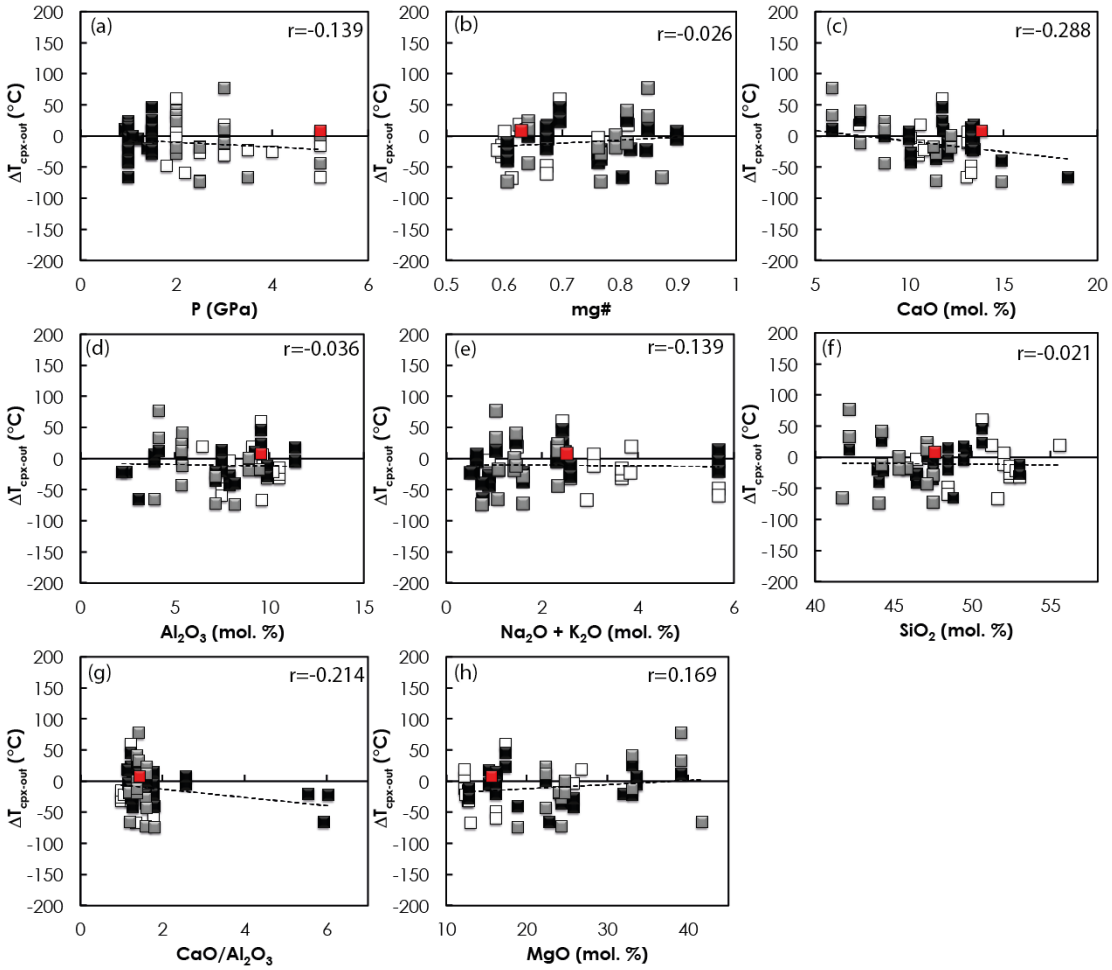

Figure S10. $\Delta T_{cpx\text{-}out}$ (experimental $T_{cpx\text{-}out}$ – calculated $T_{cpx\text{-}out}$ using Melt-PX) vs. (a) *P*, (b) bulk Mg#, (c) bulk CaO, (d) bulk Al_2O_3, (e) bulk (Na_2O+K_2O), (f) bulk SiO_2, (g) bulk molar CaO/Al_2O_3, and (h) bulk MgO; all oxides values are in mol.%. Dashed line in each panel is a least-squares fit to the points; r is the correlation coefficient. Black squares are for sets of experiments performed at < 1.7 GPa, white squares are for experiment sets performed above 1.7 GPa on SE pyroxenites, grey squares are for experiment sets performed above 1.7 GPa on SD pyroxenites, and red squares are experiments performed at 3 and 5 GPa on the bimineralogic eclogite B-ECL1 [*Kogiso and Hirschmann*, 2006].

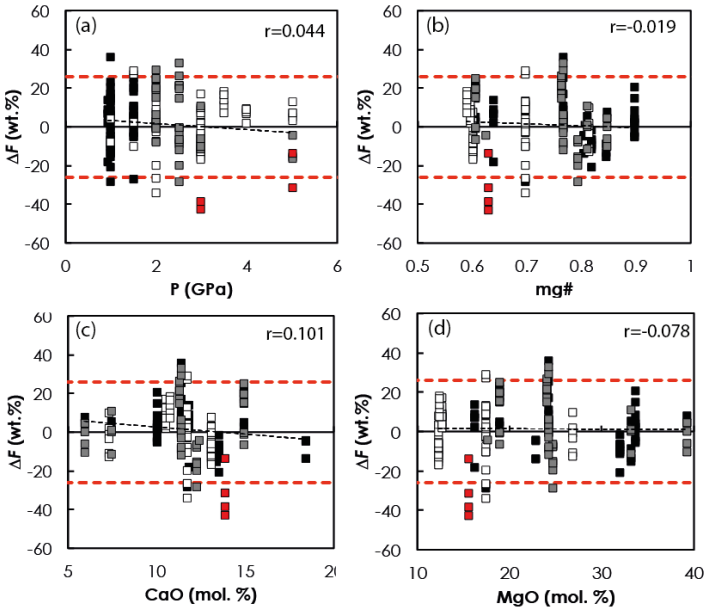

Figure S11. Δ*F* (experimental *F* – calculated *F* using Melt-PX) vs. (a) *P*, (b) bulk Mg#, (c) bulk CaO, and (d) bulk MgO; all oxides values are in mol.%. Dashed line in each panel is a least-squares fit to the points; r is the correlation coefficient. Black squares are for experiment sets performed at < 1.7 GPa, white squares are for experiments sets performed above 1.7 GPa on SE pyroxenites, grey squares are for experiments sets performed above 1.7 GPa on SD pyroxenites, and red squares are experiments performed at 3 and 5 GPa on the bimineralogic eclogite B-ECL1 [*Kogiso and Hirschmann*, 2006]. The dashed red lines show the model uncertainty (±2 SEE).

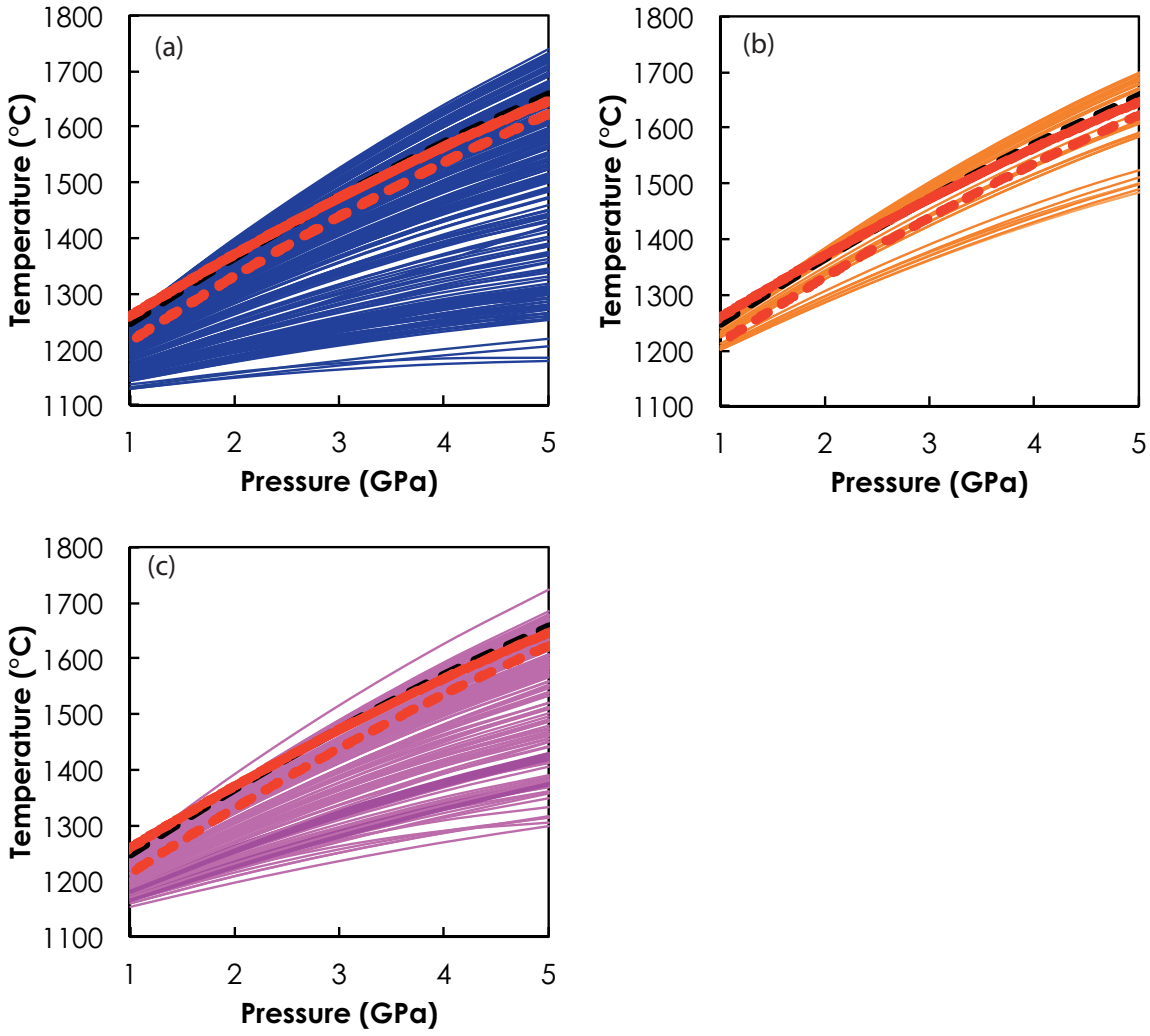

Figure S12. *F* = 5% isopleths calculated with Melt-PX for natural pyroxenites found in ophiolites and ultramafic massif (a), as xenoliths in OIBs (b), and from continental settings (c). [See Fig. 1 in *Lambart et al,* 2009a for references.] The dashed and solid red lines represent the parameterized solidus and $T_{5\%}$ isopleth from *Katz et al.* [2003], calibrated using experiments on peridotite and MgO-rich pyroxenite compositions with Na_2O and K_2O contents of 0.08–1.52 and ~0–0.14 wt.%, respectively. The dashed black line (partially hidden by the solid red line) is the parameterized solidus for peridotites with ~0.2-0.4 and ~0.03-0.05 wt.% Na_2O and K_2O [see "recommended fit" in Table 2, *Hirschmann*, 2000].

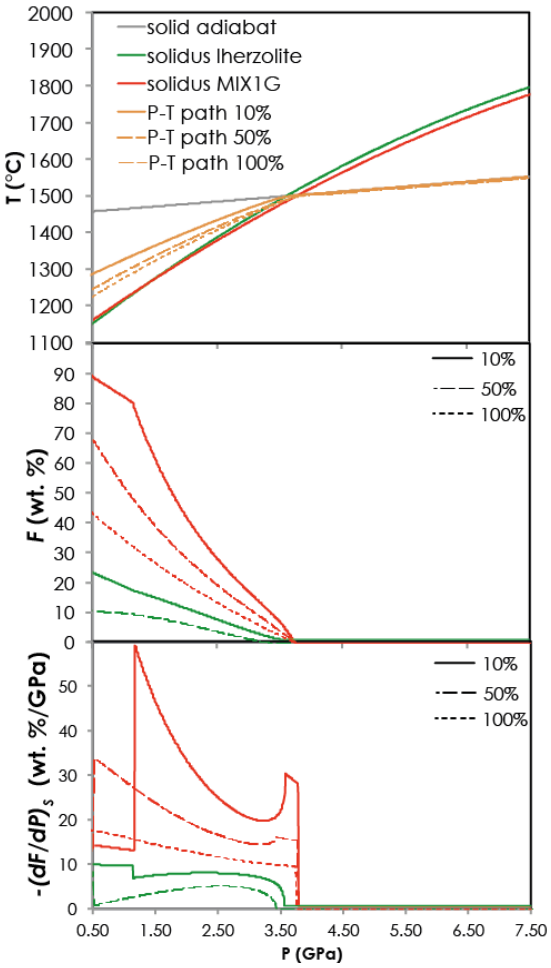

Figure S13. Results of model melting calculations of a heterogeneous mantle with 10%, 50% and 100% pyroxenite MIX1G as a distinct lithology at a potential temperature (T_P) of 1450°C. (top panel) Pressure-temperature paths for the column of mantle undergoing isentropic decompression. Mantle *P-T* paths are indicated by the orange lines, solidi are marked by the red and the green lines for MIX1G and fertile peridotite, respectively. (middle panel) Extent of melting of MIX1G (red) and fertile peridotite (green) along the adiabatic paths. (bottom panel) Melt productivity $-(dF/dP)_S$ of MIX1G (red) and fertile peridotite (green) along the corresponding adiabatic path.

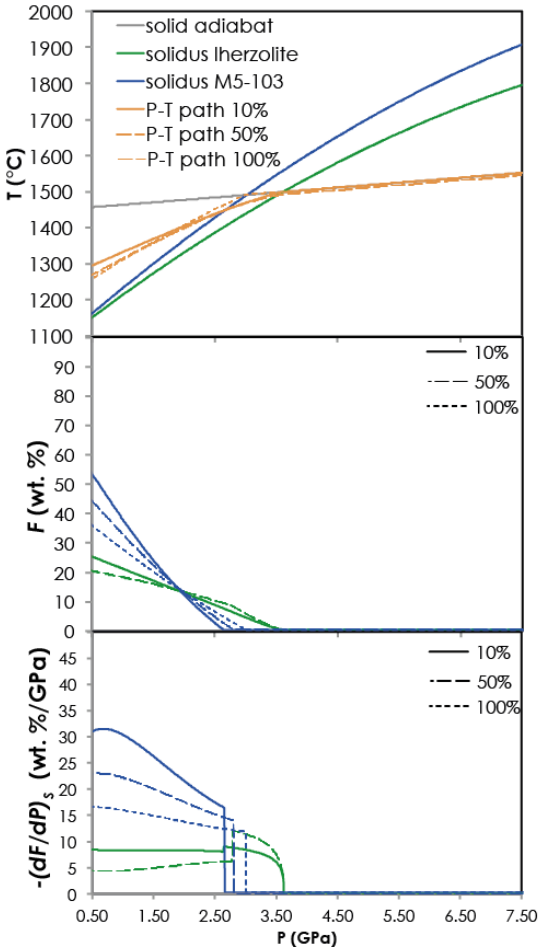

Figure S14. Results of model melting calculations of a heterogeneous mantle with 10%, 50% and 100% pyroxenite M5-103 as a distinct lithology at a potential temperature (T_P) of 1450°C. (top panel) Pressure-temperature paths for the column of mantle undergoing isentropic decompression. Mantle *P-T* paths are indicated by the orange lines, solidi are marked by the blue and the green lines for M5-103 and fertile peridotite, respectively. (middle panel) Extent of melting of M5-103 (blue) and fertile peridotite (green) along the adiabatic paths. (bottom panel) Melt productivity $-(dF/dP)_S$ of M5-103 (blue) and fertile peridotite (green) along the corresponding adiabatic path.

Table S2. Parameters used in modeling adiabatic melting

Input parameters	MIX1G	M5-103	G2	KG2	Fertile peridotite
Mass fraction cpx					0.15
Heat capacity (Cp)[a]	1090	1130	1045	1140	1190
Thermal expansivity[b]	0.00003	0.00003	0.00003	0.00003	0.00003
Density of solid	3450[e]	3350[f]	3550[c]	3400[d]	3300[c]
Entropy of fusion[g]	360	375	350	380	395
Density of liquid	2900	2900	2900	2900	2900

[a] C_p = 3R/Mmol where R is the ideal gas constant (8.314 J/(mol °C)) and Mmol is the molecular weight (kg/mol) of each lithology [*Phipps Morgan*, 2001]
[b] the thermal expansivity is assumed to be the same for all lithologies [*Phipps Morgan*, 2001]
[c] *Shorttle and Maclennan* [2011]
[d] Chosen to lie between G2 and fertile peridotite
[e] Chosen to lie between between G2 and KG2
[f] Chosen to lie between between KG2 and the fertile peridotite
[g] ΔS_f = 1R/Mmol (i.e., ΔS_f of enstatite and diopside at their 1-atm melting temperatures) [*Steebins et al.*, 1984]

Supporting references.

Albarède, F., and A. Provost (1977), Petrological and geochemical mass-balance equations: an algorithm for least-square fitting and general error analysis, *Computers & Geosciences*, *3*(2), 309–326.

Asimow, P. D., and M. S. Ghiorso (1998), Algorithmic modifications extending MELTS to calculate subsolidus phase relations, *American Mineralogist*, *83*(9-10), 1127–1132.

Asimow, P. D., M. M. Hirschmann, M. S. Ghiorso, M. J. O'Hara, and E. M. Stolper (1995), The effect of pressure-induced solid-solid phase transitions on decompression melting of the mantle, *Geochimica et Cosmochimica Acta*, *59*(21), 4489–4506.

Asimow, P. D., M. M. Hirschmann, and E. M. Stolper (1997), An analysis of variations in isentropic melt productivity, *Philosophical Transactions of the Royal Society of London A: Mathematical, Physical and Engineering Sciences,* 355(1723), 255-281.

Baker, M. B., and E. M. Stolper (1994), Determining the composition of high-pressure mantle melts using diamond aggregates, *Geochimica et Cosmochimica Acta*, *58*(13), 2811–2827.

Bartels, K., R. Kinzler, and T. Grove (1991), High pressure phase relations of primitive high-alumina basalts from Medicine Lake volcano, northern California, *Contributions to Mineralogy and Petrology*, *108*(3), 253–270.

Berman, R. G., and A. M. Koziol (1991), Ternary excess properties of grossular-pyrope-almandine garnet and their influence in geothermobarometry, *American Mineralogist*, *76*(7-8), 1223–1231.

Brown, E. L., and C. E. Lesher (2014), North Atlantic magmatism controlled by temperature, mantle composition and buoyancy, *Nature Geoscience*, *7*(11), 820–824.

Draper, D., and A. D. Johnston (1992), Anhydrous PT phase relations of an Aleutian high-MgO basalt: an investigation of the role of olivine-liquid reaction in the generation of arc high-alumina basalts, *Contributions to Mineralogy and Petrology*, *112*(4), 501–519.

Elthon, D., and C. M. Scarfe (1984), High-pressure phase equilibria of a high-magnesia basalt and the genesis of primary oceanic basalts, *American Mineralogist*, *69*(1-2), 1–15.

Fujii, T., and H. Bougault (1983), Melting relations of a magnesian abyssal tholeiite and the origin of MORBs, *Earth and Planetary Science Letters*, *62*(2), 283–295.

Gale, A., C. A. Dalton, C. H. Langmuir, Y. Su, and J.-G. Schilling (2013), The mean composition of ocean ridge basalts, Geochemistry, Geophysics, Geosystems, 14(3), 489–518. doi:10.1029/2012GC004334

Ghiorso, M. S., M. M. Hirschmann, P. W. Reiners, V. C. Kress III, (2002) The pMELTS: A revision of MELTS for improved calculation of phase relations and major element partitioning related to partial melting of the mantle to 3 GPa, *Geochemistry Geophysics Geosystems*, 3(5), 10.1029/2001GC000217.

Herzberg, C. (2006), Petrology and thermal structure of the Hawaiian plume from Mauna Kea volcano, *Nature*, *444*, 605–609.

Herzberg, C., M. Feigenson, C. Skuba, and E. Ohtani (1988), Majorite fractionation recorded in the geochemistry of peridotites from South Africa, Nature, 332(6167), 823–826.

Hirschmann, M. M. (2000), Mantle solidus: Experimental constraints and the effects of peridotite composition, *Geochemistry Geophysics Geosystems*, *1*, Paper number: 2000GC000070.

Hirschmann, M. M., and E. M. Stolper (1996), A possible role for garnet pyroxenite in the origin of the "garnet signature" in MORB, *Contributions to Mineralogy and Petrology*, 124(2), 185–208.

Hirschmann, M. M., T. Kogiso, M. B. Baker, and E. M. Stolper (2003), Alkalic magmas generated by partial melting of garnet pyroxenite, *Geology*, *31*(6), 481–484.

Jennings, E. S., and T. J. B. Holland (2015), A simple thermodynamic model for melting of peridotite in the system NCFMASOCr, *Journal of Petrology*, *56*(5), 869-892.

Katz, R. F., M. Spiegelman, and C. H. Langmuir (2003), A new parameterization of hydrous mantle melting, *Geochemistry Geophysics Geosystems*, *4*, 1073.

Keshav, S., G. H. Gudfinnsson, G. Sen, and Y. Fei (2004), High-pressure melting experiments on garnet clinopyroxenite and the alkalic to tholeiitic transition in ocean-island basalts, *Earth and Planetary Science Letters*, *223*(3-4), 365–379.

Kogiso, T., and M. M. Hirschmann (2001), Experimental study of clinopyroxenite partial melting and the origin of ultra-calcic melt inclusions, *Contributions to Mineralogy and Petrology*, *142*(3), 347–360.

Kogiso, T., and M. M. Hirschmann (2006), Partial melting experiments of bimineralic eclogite and the role of recycled mafic oceanic crust in the genesis of ocean island basalts, *Earth and Planetary Science Letters*, *249*(3-4), 188–199.

Kogiso, T., K. Hirose, and E. Takahashi (1998), Melting experiments on homogeneous mixtures of peridotite and basalt: application to the genesis of ocean island basalts, *Earth and Planetary Science Letters*, *162*(1-4), 45–61.

Kogiso, T., M. M. Hirschmann, and D. J. Frost (2003), High-pressure partial melting of garnet pyroxenite: possible mafic lithologies in the source of ocean island basalts, *Earth and Planetary Science Letters*, *216*(4), 603–617.

Kogiso, T., M. M. Hirschmann, and M. Pertermann (2004a), High-pressure partial melting of mafic lithologies in the mantle, *Journal of Petrology*, *45*(12), 2407–2422.

Lambart, S., D. Laporte, and P. Schiano (2009a), An experimental study of pyroxenite partial melts at 1 and 1.5 GPa: Implications for the major-element composition of Mid-Ocean Ridge Basalts, *Earth and Planetary Science Letters*, *288*(1-2), 335–347.

Lambart, S., D. Laporte, A. Provost, and P. Schiano (2012), Fate of pyroxenite-derived melts in the peridotitic mantle: Thermodynamical and experimental constraints, *Journal of Petrology*, *53*(3), 451–476.

Lambart, S., D. Laporte, and P. Schiano (2013), Markers of the pyroxenite contribution in the major-element compositions of oceanic basalts: Review of the experimental constraints, *Lithos*, *160–161*(0), 14–36.

Laporte, D., M. Toplis, M. Seyler, and J.-L. Devidal (2004), A new experimental technique for extracting liquids from peridotite at very low degrees of melting: application to partial melting of depleted peridotite, *Contributions to Mineralogy and Petrology*, *146*(4), 463–484.

Maaløe, S. (2004), The PT-phase relations of an MgO-rich Hawaiian tholeiite: the compositions of primary Hawaiian tholeiites, *Contributions to Mineralogy and Petrology*, *148*(2), 236–246.

O'Hara, M. J. (1972), Data reduction and projection schemes for complex compositions, in Progress in experimental petrology: Third Progress Report of Research Supported by N.E.R.C., pp. 103–126, edited by G. M Biggar, Edinburgh and Manchester Universities.

Pertermann, M., and M. M. Hirschmann (2003a), Partial melting experiments on a MORB-like pyroxenite between 2 and 3 GPa: Constraints on the presence of pyroxenite in basalt source regions from solidus location and melting rate, *Journal of Geophysical Research*, 108(B2), 2125, doi:10.1029/2000JB000118.

Pertermann, M., and M. M. Hirschmann (2003b), Anhydrous partial melting experiments on MORB-like eclogite: Phase relations, phase compositions and mineral–melt partitioning of major elements at 2–3 GPa, *Journal of Petrology*, *44*(12), 2173–2201.

Phipps Morgan, J. (2001), Thermodynamics of pressure release melting of a veined plum pudding mantle, *Geochemistry, Geophysics, Geosystems*, *2*, Paper number: 2000GC000049.

Pickering-Witter, J., and A. D. Johnston (2000), The effects of variable bulk composition on the melting systematics of fertile peridoditic assemblages, *Contributions to Mineralogy and Petrology*, *140*, 190–211.

Putirka, K., H. Mikaelian, F. Ryerson, and H. Shaw (2003), New clinopyroxene-liquid thermobarometers for mafic, evolved, and volatile-bearing lava compositions, with applications to lavas from Tibet and the Snake River Plain, Idaho, *American Mineralogist*, *88*, 1542–1554.

Shorttle, O., and J. Maclennan (2011), Compositional trends of Icelandic basalts: Implications for short–length scale lithological heterogeneity in mantle plumes, *Geochemistry, Geophysics, Geosystems*, 12, Q11008, doi:10.1029/2011GC003748.

Sleep, N. H. (1984), Tapping of magmas from ubiquitous mantle heterogeneities: An alternative to mantle plumes, *Journal of Geophysical Research, 89*, 10,029–10,041.

Snedecor, G. W., and W. G. Cochran (1989), Statistical methods. *Ames: Iowa State University Press*, xiv, 593.

Sobolev, A. V., A.W. Hofmann, D. V. Kuzmin, G. M.,Yaxley, N. T. Arndt, S.-L. Chung, L. V. Danyushevsky, T. Elliott, F. A. Frey, M. O. Garcia, A. A. Gurenko, V. S. Kamenetsky, A. C. Kerr, N. A. Krivolutskaya, V. V. Matvienkov, I. K. Nikogosian, A. Rocholl, I. A. Sigurdsson, N. M. Sushchevskaya, and M. Teklay (2007), The amount of recycled crust in sources of mantle-derived melts, Science, 316(5823), 412–417.

Spandler, C., G. M. Yaxley, D. H. Green, and A. Rosenthal (2008), Phase relations and melting of anhydrous K-bearing eclogite from 1200 to 1600°C and 3 to 5 GPa, *Journal of Petrology*, *49*(4), 771–795.

Steebins, J. F., I. S. E. Carmichael, and L. K. Moret (1984), Heath capacities and entropies of silicate liquids and glasses, *Contributions to Mineralogy and Petrology*, *86*, 131–148.

Stolper, E. M., and P. D. Asimow (2007), Insights into mantle melting from graphical analysis of one-component systems, *American Journal of Science, 307*(8), 1051–1139.

Takahashi, E., K. Nakajima, and T. L. Wright (1998), Origin of the Columbia River basalts: melting model of a heterogeneous plume head, *Earth and Planetary Science Letters*, *162*, 63–80.

Tsuruta, K., and E. Takahashi (1998), Melting study of an alkali basalt JB-1 up to 12.5 GPa: behavior of potassium in the deep mantle, *Physics of the Earth and Planetary Interiors*, *107*(1-3), 119–130.

Tuff, J., E. Takahashi, and S. A. Gibson (2005), Experimental constraints on the role of garnet pyroxenite in the genesis of high-Fe mantle plume derived melts, *Journal of Petrology*, *46*(10), 2023–2058.

Whitaker, M. L., H. Nekvasil, D. H. Lindsley, and N. J. Difrancesco (2007), The role of pressure in producing compositional diversity in intraplate basaltic magmas, *Journal of Petrology*, *48*(2), 365–393.

White, R. S., D. McKenzie, and K. O'Nions (1992), Oceanic crustal thickness from seismic measurements and rare earth element inversions, *Journal of Geophysical Research, 97*(B13), 19,683–619,715.

Yasuda, A., T. Fujii, and K. Kurita (1994), Melting phase relations of an anhydrous mid-ocean ridge basalt from 3 to 20 GPa: Implications for the behavior of subducted oceanic crust in the mantle, *Journal of Geophysical Research: Solid Earth*, *99*(B5), 9401–9414.

Yaxley, G. M., and D. H. Green (1998), High-pressure melting experiments on garnet clinopyroxenite and the alkalic to tholeiitic transition in ocean-island basalts, *Schweizerische Mineralogische und Petrographische Mitteilungen*, *78*(2), 243–255.